Dynamic behavior of a hydraulic crane operating a freely suspended payload

Bozhidar GRIGOROV, Rosen MITREV[†‡]

(*Logistics Engineering Department, Mechanical Engineering Faculty, Technical University, Sofia 1000, Bulgaria*)

[†]E-mail: rosenm@tu-sofia.bg

Abstract: We describe an investigation of the dynamic behavior of a hydraulically driven crane with a freely suspended payload during luffing and slewing motions. To simplify the task, the two movements are considered separately. Taking into account only one motion at a time, the crane is regarded as a three-link kinematic chain with revolute joints. The forward dynamics problem is solved for a crane with three rotational degrees of freedom, two of which describe the load swinging. In both the cases studied, the links are driven by a torque applied via a hydraulic drive, i.e., a linear actuator for the luffing case and a rack and pinion mechanism for the slewing motion. To compose the set of differential equations for the forward dynamics problem, a method based on a general Newton-Euler algorithm is used. From these simulations the time histories of various parameters, namely the swinging angles, hydraulic pressures, and joint forces, are determined. The results obtained via simulations are confirmed experimentally and a good agreement between the two outputs is observed. The results also show that a hydraulic drive system using fast opening flow direction control valves increases the load swing and imposes extensive inertial forces and problems of fatigue and reliability.

Key words: Hydraulic crane; Load swinging; Newton-Euler method; Hydraulic drive
http://dx.doi.org/10.1631/jzus.A1600292　　　　　　　　　**CLC number:** TH161

1 Introduction

Hydraulically driven cranes are materials-handling equipment used in many areas where compact devices are needed to manipulate heavy loads, typically in automobile, railroad, or sea transport. Dynamical modeling of hydraulic cranes is essential for their designers because of the need to reduce manufacturing costs and to gain better insight over the behavior of the designed mechanical system. An adequate dynamic model and accurate model parameters are necessary prerequisites for a proper design as well as fatigue strength and reliability predictions when dynamically loaded structures are considered (Troha *et al.*, 2015). Such a model has to treat a crane as a multibody system and to take into account the dynamical properties of the driving mechanisms. This increases the complexities of both the models and the numerical problems during the integration of the equations of motion.

In many cases, these installations feature articulated booms with three to five degrees of freedom, which additionally increase the flexibility and allow payloads to be moved in limited, closed volumes. Attachment of the payload to the boom can be either fixed by some kind of a gripper, or it may be suspended from a gripping device by cables if no particular orientation of the payload in space is required. In the latter case, the payload becomes a pendulum-type device and the balance during motion is impaired, causing some control and positioning problems. Obviously, the swinging payload can affect the machine itself or/and the handling operations. First, for automatic loading and unloading systems, or with an operator without much experience, this phenomenon

---

[‡] Corresponding author

ⓘ ORCID: Bozhidar GRIGOROV, http://orcid.org/0000-0002-7412-2858; Rosen MITREV, http://orcid.org/0000-0001-6276-1225

considerably increases the crane cycle time. Second, the load swinging imposes particular dynamical loading on the crane elements, generating additional inertia forces and torques, causing increased stress and irregularity in motion. In the case of jib cranes, payload sway can also be caused by other reason-hitting obstacles, lifting the payload from the ground with initially slack slings or other such factors. In any case, moving the boom along some trajectory in space causes the payload to swing freely about the pivot point due to unavoidable tangential and radial accelerations. This is especially true for hydraulic drive, when the sudden opening or closure of manually or electromagnetically controlled valves occurs, and a sudden surge of pressure is observed (Jovanovic *et al.*, 2014).

Payload-swinging during crane-boom slewing or luffing has been the subject of many academic and industrial interdisciplinary research activities involving the fields of mechanical, electrical, and control engineering. Some basic textbooks (Divisiev, 1986; Vaynson, 1989) pay attention to the payload oscillations for cranes driven by a slewing mechanism with flexible joints, in order to determine the necessary torque and motor power depending on the payload-swinging and the flexibility of the driveline elements. In other studies, investigations were aimed at finding the inertial forces acting upon the boom and other parts of the structure (Jerman, 2006; Marinovic *et al.*, 2012). Another direction of research is the possibility of developing strategies for controlling the slewing motion, in order to damp the payload swing and thus to reduce the dynamic forces and increase the performance of the system. This direction is also applicable to the horizontal translation as well as to the hoist mechanism (Abdel-Rahman *et al.*, 2003; Palis and Palis, 2008; Lawrence and Singhose, 2010; Devesse, 2012; Gudarzi, 2016).

Crane-system modeling methods presented in some studies are based upon fundamental mechanical principles, but vary to a certain extent. For derivation of the governing equations, Divisiev (1986) used Newton's second law of motion, while Marinovic *et al.* (2012) used a mathematical model based on second-order Lagrange equations defined for a multibody system. In all cases, the elasticity and damping of the steel structure, the friction in the main bearing, and the nonlinearity of the power transmission can be

easily taken into account for better accuracy. Papadopoulos and Sarkar (1997) used the well-known Newton-Euler iterative method, implemented symbolically, to derive equations of motion for the investigated mechanical system. After reviewing the crane models available in the literature, such as distributed- and lumped-mass, Abdel-Rahman *et al.* (2003) analyzed the reduced models as a special case of spatial pendulum ones. In this case, an approximate solution is available through the method of multiple scales. A few authors have explored the crane system by considering the elasticity of the metal structure. Ju *et al.* (2006) have studied the dynamic response of tower cranes coupled with the pendulum motions of the payload. The tower crane was modeled using the finite element method, while the pendulum motion was represented as rigid-body kinetics. Ren *et al.* (2008) have derived the governing equations for the dynamic response of a crane ship coupled with a pendulum motion of the payload. The developed boom model was based on the finite element method, while the payload was considered as a planar pendulum of point mass. The dynamic response was studied using numerical methods. In all cases, the considerable escalation of the calculations needed with the increasing number of bodies cannot be avoided, but reliable results were obtained.

The literature survey reveals a variety of simplifications made in the mathematical models, such as considering small angles of the payload sway (Ju *et al.*, 2006) and a non-deformable structure (Chin *et al.*, 2001), which serve to set and solve the problems with sufficient accuracy within the modeling aims.

A practical approach, widely used in engineering practice for simulation of the multibody systems, is a modeling by way of general purpose numeric multibody codes (Gruening *et al.*, 2010). This type of software usually has a high license cost and the received results are limited by its capabilities. Another drawback is that the generated equations of motion are embedded in the program and are not available for review and modification by the user. In some cases, simultaneous modeling and simulation of subsystems from different physical domains is impossible, and thus co-simulation and interface for data exchange between different dedicated programs are necessary (Sicklinger *et al.*, 2014).

The investigations described are, however, directed mostly towards tower, gantry, harbor, or mobile cranes with long reach and electric driving mechanisms (Marinković *et al.*, 2012). The influence of payload swinging on the hydraulic system has not been investigated in depth. Since the hydraulic system has its own dynamics due to fluid compressibility, it is necessary also to consider its effect on the overall dynamic performance of the crane. Hydraulic drives impose specific elements and require a slightly different mathematical approach due to the specificity of the driving system itself. This is taken into account by some authors (Sun *et al.*, 2005; Sun and Liu, 2006) and directed towards hydraulically driven luffing mechanisms in boom cranes. A hydraulic system model also can be combined with a low-order dynamic model for multilink flexible cranes, and is suitable for a deeper understanding of the mechanical system (Linjama and Virvalo, 1999). Other combined models are suitable for simulation of the machine response and sizing of the hydraulic components (Papadopoulos and Sarkar, 1997).

The general aim of the present study is to investigate the dynamic behavior of a hydraulically driven crane with an articulated boom and a freely suspended payload at its end. The investigation is directed towards the worst case of hydraulic flow control, i.e., sudden opening and closure of hydraulic valves. To simplify the problem, two motions of the crane boom, namely luffing and slewing, are considered separately. This generally reduces the case to the dynamics of luffing jib cranes and slewing cranes.

2 System model

2.1 General model of the mechanical system

Fig. 1 shows a discrete 3D model of a hydraulic rotating crane with an articulated boom and a freely suspended payload. The crane consists of a fixed base and three rotating links. The column rotates about the vertical axis and the boom is composed of an arm and a forearm, both rotating about horizontal axes to determine the reach of the crane and the payload lift respectively. To simulate the spatial sway of the payload, two additional rotational joints are added to the forearm, both having mutually perpendicular axes of rotation. The crane hydraulic drive system consists

of a rack and pinion mechanism, intended for column rotation, and hydraulic cylinders, intended for arm and forearm rotation. All crane elements are considered as rigid.
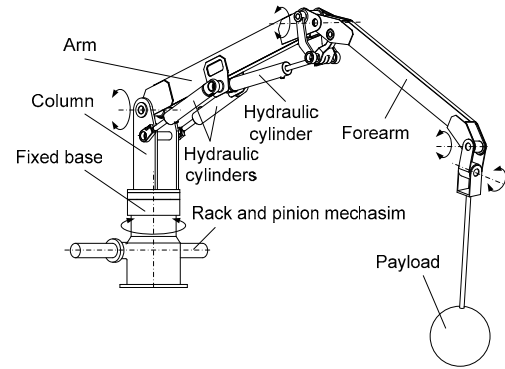
Fig. 1 Discrete 3D model of the hydraulic crane

Taking into consideration slewing and luffing motions separately, the crane is regarded as a three-link kinematic chain with three revolute joints. Investigating the dynamic behavior of such a kinematic chain requires the solution of the forward dynamics problem for a mechanism with three rotational degrees of freedom, driven by a torque at the first joint, calculated according to some law. Among the many different approaches, one solution of such a problem is to derive a set of second-order differential equations in a form similar to that proposed by Vukobratovic and Potkonjak (1982):

$$-\boldsymbol{M}(\boldsymbol{\theta})\ddot{\boldsymbol{\theta}} - \boldsymbol{H}(\boldsymbol{\theta},\dot{\boldsymbol{\theta}}) + \boldsymbol{G}(\boldsymbol{\theta}) + \boldsymbol{\tau}(t) = \mathbf{0}, \qquad (1)$$

where $\boldsymbol{\theta}$, $\dot{\boldsymbol{\theta}}$, and $\ddot{\boldsymbol{\theta}}$ are respectively the vectors of position, velocity, and angular acceleration in the joints (generalized coordinates); $\boldsymbol{M}(\boldsymbol{\theta})$ is the mass matrix composed of elements defining the acceleration terms $\ddot{\boldsymbol{\theta}}$ for each joint; $\boldsymbol{H}(\boldsymbol{\theta},\dot{\boldsymbol{\theta}})$ is a matrix composed of elements defining the acceleration terms, but not containing $\ddot{\boldsymbol{\theta}}$; $\boldsymbol{G}(\boldsymbol{\theta})$ is the weight term; and $\boldsymbol{\tau}(t)$ is the driving torque vector at each joint.

To compose the set of differential equations of motion, a non-iterative method proposed in Grigorov (2013) is used. The method is based on a general Newton-Euler algorithm for solving the forward dynamics problem of an open kinematic chain with

revolute joints. It is based on D'Alembert's principle, which implies that the dynamic balance of each link j (Fig. 2) is considered during the entire motion and with all the forces and moments acting on the link, including inertial, gravity, and the actuator torque.
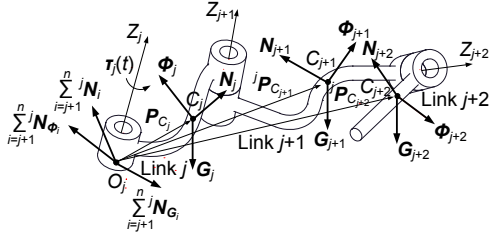
Fig. 2 Local frames and forces acting on the kinematic chain links

This method regards the links of the kinematic chain as rigid bodies and requires a frame attached to each link according to some known principle. In the present investigation, a Denavit-Hartenberg (D-H) notation (Hartenberg and Denavit, 1955) is used. According to D'Alembert's principle and the notations in Fig. 2, summing all the moments at the origin of the jth frame yields

$$-N_{\Phi_j} - N_j + N_{G_j} - \sum_{i=j+1}^{n} {}^{j}N_{\Phi_i} - \sum_{i=j+1}^{n} {}^{j}N_i$$
$$+ \sum_{i=j+1}^{n} {}^{j}N_{G_i} + \tau_j(t) = 0, \qquad (2)$$

where N_{Φ_j} is a moment with respect to the frame origin of the inertial force acting on the link at the center of gravity due to the linear acceleration of the link, N_j is an inertial moment acting on the link due to the angular acceleration, N_{G_j} is the moment of the gravity force (the weight of the link) acting at the center of gravity C_j with respect to the frame origin, ${}^{j}N_{\Phi_i}$, ${}^{j}N_i$, and ${}^{j}N_{G_i}$ are moments of inertial force, inertial moment, and moment of the gravity force acting on link i, respectively, expressed in terms of frame j and reduced to the origin of frame j ($j<i\leq n$), $\tau_j(t)$ is the joint torque (usually time or position dependent) exerted by the actuator at joint j.

Inertial forces Φ_j and moments N_j acting at the center of gravity of each link can be calculated using the well-known Newton-Euler equations (Craig, 2005):

$$\Phi_j = m_j \dot{v}_{C_j}, \qquad (3)$$

$$N_j = I_j \dot{\omega}_j + \omega_j \times I_j \omega_j, \qquad (4)$$

where $\dot{v}_{C_j}$ is the linear acceleration of the gravity center of link j expressed with respect to the link frame, ω_j and $\dot{\omega}_j$ are the angular velocity and acceleration of frame j expressed with respect to the same frame, m_j and I_j are the mass and inertia tensor of link j written with respect to a frame with origin located at the center of gravity C_j and with the same orientation as the link frame j.

Using Eqs. (3) and (4), and after some symbolic transformations and simplifications, Eq. (2) can be rewritten in the following form:

$$-\sum_{i=j}^{n} \left(m_j \, {}^{j}P_{C_i} \times {}^{j}R_i \dot{v}_{C_i} \right) - \sum_{i=j}^{n} I_i \, {}^{j}R_i \dot{\omega}_i$$
$$-\sum_{i=j}^{n} {}^{j}R_i (\omega_i \times I_i \omega_i) + \sum_{i=j}^{n} \left({}^{j}P_{C_i} \times {}^{j}R_0 G_i \right) + \tau_j(t) = 0, \qquad (5)$$

where ${}^{j}P_{C_i}$ is the position of the gravity center of link i expressed in terms of the jth frame, P_{C_i} is the position of the gravity center of link i expressed in the same frame, G_i is the weight of the link expressed in terms of the 0th frame, and ${}^{j}R_i$ is the following 3×3 rotational matrix:

$$ {}^{j}R_i = \begin{bmatrix} \cos\theta_i & -\sin\theta_i & 0 \\ \sin\theta_i & \cos\theta_i & 0 \\ 0 & 0 & 1 \end{bmatrix}, \qquad (6)$$

describing the orientation of frame i with respect to frame j.

Starting from frame 0, which has zero velocities and accelerations, $\dot{v}_{C_j}$ and $\dot{\omega}_j$ are evaluated by the following formulas (Grigorov, 2013):

$$\omega_j = \sum_{i=1}^{j} {}^{j}R_i \dot{\theta}_j, \qquad (7)$$

$$\dot{\omega}_j = \sum_{i=1}^{j} {}^{j}R_i \ddot{\theta}_i + C_{\varepsilon_j}, \qquad (8)$$

$$\dot{v}_j = \sum_{i=1}^{j-1} \left[{}^{j}R_i \ddot{\theta}_i \times \left(-{}^{j}P_i \right) \right] + C_{V_j}, \qquad (9)$$

$$\dot{v}_{C_j} = \sum_{i=1}^{j} \left[{}^{j}\!R_i \ddot{\theta}_i \times \left(-{}^{j}\!P_i + P_{C_j} \right) \right] + C_{VC_j}. \tag{10}$$

The separated members in Eqs. (8)–(10) for *j*>1, which do not contain angular accelerations of the joints are

$$C_{\varepsilon_j} = {}^{j}\!R_{j-1} C_{\varepsilon_{j-1}} + {}^{j}\!R_{j-1}\omega_{j-1} \times \dot{\theta}_j, \tag{11}$$

$$C_{V_j} = {}^{j}\!R_{j-1}\left[C_{\varepsilon_{j-1}} \times P_j + \omega_{j-1} \times \left(\omega_{j-1} \times P_j \right) + C_{V_{j-1}} \right], \tag{12}$$

$$C_{VC_j} = C_{\varepsilon_j} \times P_{C_j} + \omega_j \times \left(\omega_j \times P_{C_j} \right) + C_{V_j}. \tag{13}$$

In Eqs. (7)–(13), $\ddot{\theta}_i$ ($\ddot{\theta}_i = \begin{bmatrix} 0 & 0 & \ddot{\theta}_i \end{bmatrix}^{T}$) is the angular acceleration of frame *i* and similar definitions are given for $\dot{\theta}_i$ and θ_i; C_{ε_j}, C_{V_j}, and C_{VC_j} are elements, correspondingly, of the angular acceleration, link frame origin linear acceleration, and link gravity center linear acceleration, which do not depend on $\ddot{\theta}_j$; ${}^{j}\!P_i$ and ${}^{j}\!P_{C_i}$ are position vectors specifying the origin and the gravity center of the *i*th frame expressed in terms of the *j*th frame, P_j is the vector of the (*j*+1)th frame's origin with respect to the *j*th frame.

Substituting Eqs. (7)–(13) into Eq. (5) and performing some symbolic transformations and simplifications, finally the equilibrium equations of the kinematic chain links can be derived (Eqs. (15)–(17)). The aim of the transformations is to express the left side of the equation as a matrix multiplication. For this purpose, in Eqs. (15)–(17) the vector cross product is expressed as the product of a 3×3 skew-symmetric matrix ⟨ ⟩ and a vector (Zill and Cullen, 2006); for example,

$$\left\langle {}^{j}\!P_{C_i} \right\rangle = \begin{bmatrix} 0 & -{}^{j}\!z_{C_i} & {}^{j}\!y_{C_i} \\ {}^{j}\!z_{C_i} & 0 & -{}^{j}\!x_{C_i} \\ -{}^{j}\!y_{C_i} & {}^{j}\!x_{C_i} & 0 \end{bmatrix}, \tag{14}$$

where ${}^{j}\!x_{C_i}$, ${}^{j}\!y_{C_i}$, and ${}^{j}\!z_{C_i}$ are elements of ${}^{j}\!P_{C_i}$.

$$\left(m_1 \left\langle P_{C_1} \right\rangle \left\langle -P_{C_1} \right\rangle + m_2 \left\langle {}^{1}\!P_{C_2} \right\rangle {}^{1}\!R_2 \left\langle {}^{2}\!P_1 - P_{C_2} \right\rangle {}^{2}\!R_1 \right. $$
$$\left. + m_3 \left\langle {}^{1}\!P_{C_3} \right\rangle {}^{1}\!R_3 \left\langle {}^{3}\!P_1 - P_{C_3} \right\rangle {}^{3}\!R_1 + I_1 + {}^{1}\!R_2 I_2 \, {}^{2}\!R_1 \right. $$

$$\left. + {}^{1}\!R_3 I_3 \, {}^{3}\!R_1 \right) \ddot{\theta}_1 + \left(m_2 \left\langle {}^{1}\!P_{C_2} \right\rangle {}^{1}\!R_2 \left\langle -P_{C_2} \right\rangle \right. $$
$$\left. + m_3 \left\langle {}^{1}\!P_{C_3} \right\rangle {}^{1}\!R_3 \left\langle {}^{3}\!P_2 - P_{C_3} \right\rangle {}^{3}\!R_2 + {}^{1}\!R_2 I_2 \right. $$
$$\left. + {}^{1}\!R_3 I_3 \, {}^{3}\!R_2 \right) \ddot{\theta}_2 + \left(m_3 \left\langle {}^{1}\!P_{C_3} \right\rangle {}^{1}\!R_3 \left\langle -P_{C_3} \right\rangle + {}^{1}\!R_3 I_3 \right) \ddot{\theta}_3 $$
$$= \sum_{i=1}^{3} \left({}^{1}\!P_{C_i} \times {}^{1}\!R_0 G_i \right) - \sum_{i=1}^{3} \left[{}^{1}\!R_i \left(\omega_i \times I_i \omega_i \right) \right] $$
$$- \sum_{i=2}^{3} {}^{1}\!R_i I_i C_{\varepsilon_i} - \sum_{i=1}^{3} m_i \left({}^{1}\!P_{C_i} \times {}^{1}\!R_i C_{VC_i} \right) + \tau_1(t), \tag{15}$$

$$\left(m_2 \left\langle P_{C_2} \right\rangle \left\langle {}^{2}\!P_1 - P_{C_2} \right\rangle {}^{2}\!R_1 + m_3 \left\langle {}^{2}\!P_{C_3} \right\rangle {}^{2}\!R_3 \right. $$
$$\left. \cdot \left\langle {}^{3}\!P_2 - P_{C_3} \right\rangle {}^{3}\!R_2 + I_2 + {}^{2}\!R_3 I_3 \, {}^{3}\!R_1 \right) \ddot{\theta}_1 $$
$$+ \left(m_2 \left\langle P_{C_2} \right\rangle \left\langle -P_{C_2} \right\rangle + m_3 \left\langle {}^{2}\!P_{C_3} \right\rangle {}^{2}\!R_3 \right. $$
$$\left. \cdot \left\langle {}^{3}\!P_2 - P_{C_3} \right\rangle {}^{3}\!R_2 + I_2 + {}^{2}\!R_3 I_3 \, {}^{3}\!R_2 \right) \ddot{\theta}_2 $$
$$+ \left(m_3 \left\langle {}^{2}\!P_{C_3} \right\rangle {}^{2}\!R_3 \left\langle -{}^{2}\!P_{C_3} \right\rangle + {}^{2}\!R_3 I_3 \right) \ddot{\theta}_3 $$
$$= \sum_{i=2}^{3} \left({}^{2}\!P_{C_i} \times {}^{2}\!R_0 G_i \right) - \left[\sum_{i=2}^{3} {}^{2}\!R_i \left(\omega_i \times I_i \omega_i \right) \right] $$
$$- \sum_{i=2}^{3} {}^{2}\!R_i I_i C_{\varepsilon_i} - \sum_{i=2}^{3} m_i \left({}^{2}\!P_{C_i} \times {}^{2}\!R_i C_{VC_i} \right), \tag{16}$$

$$\left(m_3 \left\langle P_{C_3} \right\rangle \left\langle {}^{3}\!P_1 - P_{C_3} \right\rangle {}^{3}\!R_1 + I_3 \, {}^{3}\!R_1 \right) \ddot{\theta}_1 $$
$$+ \left(m_3 \left\langle P_{C_3} \right\rangle \left\langle {}^{3}\!P_2 - P_{C_3} \right\rangle {}^{3}\!R_2 + I_3 \, {}^{3}\!R_2 \right) \ddot{\theta}_2 $$
$$+ \left(m_3 \left\langle P_{C_3} \right\rangle \left\langle -P_{C_3} \right\rangle + I_3 \right) \ddot{\theta}_3 $$
$$= P_{C_3} \times {}^{3}\!R_0 G_3 - \omega_3 \times I_3 \omega_3 - I_3 C_{\varepsilon_3} - m_3 \left(P_{C_3} \times C_{VC_3} \right). \tag{17}$$

Each of Eqs. (15)–(17) represents a 3×1 column vector. Because the only possible motion is the rotation about the joint local Z_i-axis, then in order to derive the set of differential equations in form (1), a dot product of Eqs. (15)–(17) and unit vectors along local Z_i=[0 0 1]^{T} axis is taken. In such a case, the vector of generalized coordinate accelerations can be written in the form $\ddot{\theta} = \begin{bmatrix} \ddot{\theta}_1 & \ddot{\theta}_2 & \ddot{\theta}_3 \end{bmatrix}^{T}$. Finally, the received set of differential equations is considered as an initial-value problem and is written in the following general form:

$$\ddot{\theta} = M^{-1}(\theta) \left[\tau(t) - H\left(\theta, \dot{\theta} \right) + G(\theta) \right], \tag{18}$$

which is convenient for solution by standard numerical routines.

2.2 Slewing case

Differential equations for the slewing case are derived from the system of equations (Eqs. (15)–(17)), for which the needed geometrical quantities are defined by the D-H parameters. In this case, link 1 is represented as a combination of the column and boom (composed from the arm and the forearm), regarded as a single body (link 1), which rotates about a vertical axis Z_0 (Fig. 3). The slewing motion is defined by its rotational angle θ_1, while the spatial motion of the payload is defined by swinging angles θ_2 and θ_3. By L_s is designated the length of the cable.
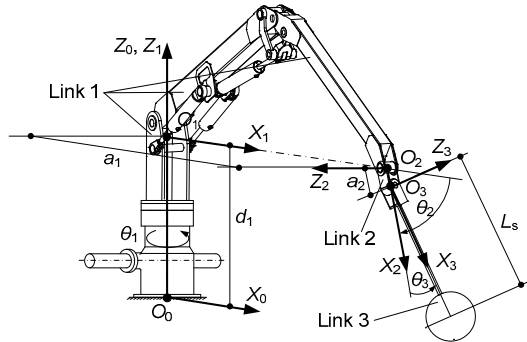

Fig. 3 Denavit-Hartenberg (D-H) parameters and frame attachment for the slewing case

The local frame attachment is depicted in Fig. 3 and the values of the corresponding D-H parameters are summarized in Table 1.

Table 1 Denavit-Hartenberg (D-H) parameters for the slewing case

Link j	α_j (rad)	a_j (m)	d_j (m)	θ_j (rad)
1	0	0	Min: −1.22; Max: 1.18	θ_1
2	$\pi/2$	Min: 2.037; Max: 3.352	0	θ_2
3	$-\pi/2$	0.162	0	θ_3

Max or min refers to the maximum or the minimum reach of the crane

The slewing motion is performed by using a standard rack and pinion mechanism, which generates a driving torque. The pinion (with radius R) is driven by the rack, which is connected to a double action hydraulic cylinder (with piston area S_1) (Fig. 4).
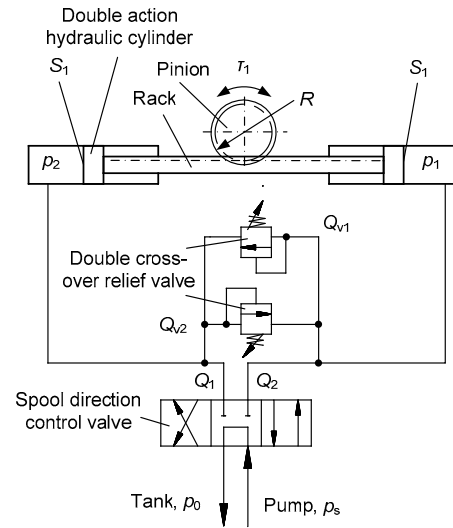

Fig. 4 Slewing hydraulic rack and pinion mechanism

The flow to the cylinder is controlled by the spool direction control valve. A double cross-over relief valve is incorporated in the hydraulic circuit, in order to relieve the excessive pressure caused by sudden closure of the direction control valve and occurred inertial loads.

The first link is driven by a torque $\boldsymbol{\tau}_1=[0\ 0\ \tau_1]^{\mathrm{T}}$. The hydraulic cylinder force and thus τ_1 can be determined using the well-known hydraulic theory (Akers *et al.*, 2006). A simplified dynamical model of the hydraulic system is presented, assuming constant supply pressure, compressible oil, and the absence of oil leakage in the hydraulic system. Based on the continuity equation for the compressible oil and referring to Fig. 4, one can write equations for the pressures in the hydraulic cylinders as follows:

$$\dot{p}_1 = \left(\frac{\beta}{V_0^1 + S_1 x_1}\right)\left(Q_1 - S_1\dot{x}_1 - Q_{v1} + Q_{v2}\right), \quad (19)$$

$$\dot{p}_2 = \left(\frac{\beta}{V_0^1 + S_1(l_1 - x_1)}\right)\left(S_1\dot{x}_1 - Q_2 + Q_{v1} - Q_{v2}\right), \quad (20)$$

where p_1 and p_2 are the pressures in the hydraulic cylinder chambers, Q_1 and Q_2 are the flow rates through the direction control valve, Q_{v1} and Q_{v2} are the flow rates through the relief valves, β is the fluid bulk modulus, V_0^1 is the constant oil volume subjected to compression, x_1 is the piston displacement,

$\dot{x}_1$ is the piston velocity, S_1 is the piston area, and l_1 is the hydraulic cylinder stroke.

The flow through the direction control valve is a nonlinear function of the pressure drop across the valve orifices and of the current orifice size (for turbulent flow):

$$Q_1 = C_d w x_v(t) \sqrt{\frac{2|p_s - p_1|}{\rho}} \text{sign}(p_s - p_1), \quad (21)$$

$$Q_2 = C_d w x_v(t) \sqrt{\frac{2|p_2 - p_0|}{\rho}} \text{sign}(p_2 - p_0), \quad (22)$$

where C_d is the orifice discharge coefficient, w is the direction control valve area gradient, $x_v(t)$ is the direction control valve opening as a function of time, ρ is the oil density, p_s is the supply pressure, p_0 is the drain pressure, and function sign is '−1' for a negative number, '0' for zero, or '+1' for a positive number.

If the dynamics of the relief valves is neglected and the turbulent flow is assumed, then the flow through the valves is governed by

$$Q_{vi} = C_{dv} A_v (\Delta p^i) \sqrt{\frac{2}{\rho}|\Delta p^i|} \text{sign}(\Delta p^i), \quad i = 1, 2, \quad (23)$$

where the pressure-dependent orifice passage area $A_v(\Delta p^i)$ is described by the following piecewise linear function:

$$A_v(\Delta p^i) = \begin{cases} 0, & \Delta p^i \le p_{set}, \\ k(\Delta p^i - p_{set}), & p_{set} < \Delta p^i < p_{max}, \\ A_{max}, & \Delta p^i \ge p_{max}, \end{cases} \quad (24)$$

$$k = \frac{A_{max}}{p_{reg}}, \quad (25)$$

where Δp^i is the relief valve pressure differential for valve i, A_{max} is the fully open relief valve passage area, p_{set} is the relief valve preset pressure, p_{reg} is the relief valve regulation range, p_{max} is the valve pressure at the maximum opening, and C_{dv} is the orifice discharge coefficient.

Using the solution of Eqs. (19) and (20), the function to determine the torque is given as

$$\boldsymbol{\tau}_1 = \begin{bmatrix} 0 & 0 & (S_1(p_1 - p_2) - b_1 \dot{x}_1)R \end{bmatrix}^T, \quad (26)$$

where b_1 is the viscous friction coefficient. Moreover, the angular velocity is

$$\dot{\boldsymbol{\theta}}_1 = \begin{bmatrix} 0 & 0 & \dfrac{\dot{x}_1}{R} \end{bmatrix}^T. \quad (27)$$

2.3 Luffing case

In this case, the payload lifting is performed by boom raising by means of arm hydraulic cylinders. The local frame attachment is depicted in Fig. 5. Here, the following assumptions are made: (1) During the luffing, the two links of the boom (the arm and the forearm) do not move with respect to each other and form a rigid link 1, rotating about the horizontal axis Z_1 (Fig. 5); (2) The column is fixed; (3) The payload is lifted at the maximum reach (the actual geometrical configuration is not shown in Fig. 5). The boom motion is defined by the rotational angle θ_1, while the spatial motion of the payload is defined by the swinging angles θ_2 and θ_3.

Table 2 summarizes the D-H parameters for the luffing case.

The boom driving moment depends on the arm hydraulic cylinder force and the geometrical parameters of its attachment to the arm and the column (Pavlovic *et al.*, 2014) (Fig. 6a).
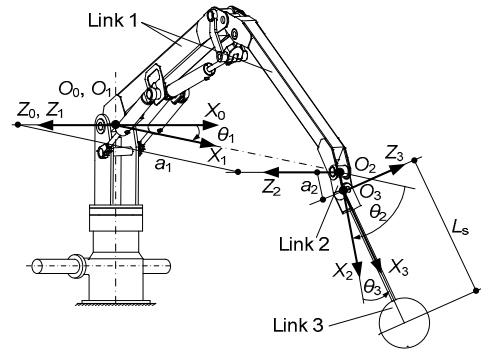

Fig. 5 Denavit-Hartenberg (D-H) parameters and frame attachment for the luffing case

Table 2 Denavit-Hartenberg (D-H) parameters for the luffing case

Link j	α_j (rad)	a_j (m)	d_j (m)	θ_j (rad)
1	0	0	0	θ_1
2	0	3.352	0	θ_2
3	$-\pi/2$	0.162	0	θ_3

The arm hydraulic cylinder is controlled by a hydraulic circuit, a fragment of which is shown in Fig. 6b. Thus, the following two equations:

$$\dot{p}_1 = \left(\frac{\beta}{V_0^2 + S_2 x_2}\right)(Q_1 - S_2 \dot{x}_2), \qquad (28)$$

$$\dot{p}_2 = \left(\frac{\beta}{V_0^2 + S_3 (l_2 - x_2)}\right)(S_3 \dot{x}_2 - Q_2), \qquad (29)$$

together with Eqs. (21) and (22), are used for pressure calculations, where p_1 and p_2 are the cap end and rod end hydraulic cylinder chamber pressures, S_2 and S_3 are the piston and piston minus rod areas, V_0^2 is the constant oil volume subjected to compression, x_2 is the piston displacement, $\dot{x}_2$ is the piston velocity, and l_2 is the hydraulic cylinder stroke.
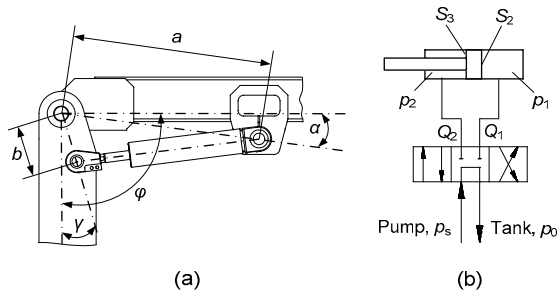

Fig. 6 Geometrical parameters of the arm
(a) Hydraulic cylinder attachment; (b) Hydraulic circuit fragment

Referring to the designations in Fig. 6, the arm driving moment is given as

$$\tau_1 = \left[\begin{array}{ccc} 0 & 0 & \dfrac{(S_2 p_1 - S_3 p_2 - b_2 \dot{x}_2) ab \sin(\varphi - \alpha - \gamma)}{\sqrt{a^2 + b^2 - 2ab\cos(\varphi - \alpha - \gamma)}} \end{array}\right]^{\mathrm{T}}, \qquad (30)$$

where φ is the current angle between links and b_2 the viscous friction coefficient. Moreover, for the angular velocity of the boom, we can write

$$\dot{\theta}_1 = \left[\begin{array}{ccc} 0 & 0 & \dfrac{\dot{x}_2 \sqrt{a^2 + b^2 - 2ab\cos(\varphi - \alpha - \gamma)}}{ab\sin(\varphi - \alpha - \gamma)} \end{array}\right]^{\mathrm{T}}. \qquad (31)$$

3 Numerical examples

Using the method described in the previous sections, the numerical simulation of an experimental crane is carried out. To confirm the results, an experimental procedure with the same crane is also conducted. The following assumptions are made: (1) The payload hoisting will not occur during slewing, as the rotation about the vertical axis is not considered during luffing motion; (2) The damping forces in joints will be neglected; (3) The mass properties of the moving parts are taken from a CAD model of a real-life crane design.

The numerical values used for the mass and mass moments of inertia of the crane elements are shown in Table 3, and the numerical values for the hydraulic system parameters are shown in Table 4. Numerical values for the geometrical parameters are as follows: L_s=1.8 m, a=0.716 m, b=0.181 m, α=7.3°, and γ=18°.

3.1 Slewing case simulation

To solve the mechanical model for the generalized coordinates θ and $\dot{\theta}$, the sets of Eqs. (15)–(17), (19), and (20) are numerically integrated simultaneously as an initial-value problem. The simulation is performed for two positions of the arms, i.e., the minimum reach and the maximum reach with the corresponding numerical values from Table 1. At the beginning of the simulation, the three angles are set to $\theta_1(0)$=0°, $\theta_2(0)$=−90°, $\theta_3(0)$=0°, and the initial pressures are set to $p_1(0)$=$p_2(0)$=4.5 MPa. The duration of the simulation is 7 s and the rotation itself is set to 5 s, after which time the valve closes.

The results of the simulation are given in Figs. 7–12. Fig. 7 shows the time history of the slewing angle θ_1, Fig. 8 shows the driving torque τ_1 exerted at the first link, and Fig. 9 shows the corresponding hydraulic cylinder pressures at the minimum reach and the maximum reach. Figs. 10 and 11 respectively show graphs of angles θ_2 and θ_3, for the minimum reach and the maximum reach. Fig. 12 shows the reactive force in the forearm driving hydraulic cylinder.

The adopted method of solution gives, after integration of Eqs. (15)–(17), a solution for $\ddot{\theta}$ and enables determination of the inertial forces and moments acting on the links, as described by Eq. (5). This approach makes the mechanical structure force

Table 3 Numerical values for the mass and mass moments of inertia of the crane elements

| Link j | Mass, m_j (kg) | | Inertia tensor I_j elements on the main diagonal (kg·m²) | |
	Luffing	Slewing	Luffing	Slewing
1	m_1=128.1	m_1=277.3	J_{xx}=1.4, J_{yy}=95, J_{zz}=94	Minimum reach: J_{xx}=65.9, J_{yy}=193.0, J_{zz}=131.0; Maximum reach: J_{xx}=41.8, J_{yy}=274.5, J_{zz}=236.2
2	m_2=5.9	m_2=5.9	J_{xx}=0.016, J_{yy}=0.032, J_{zz}=0.027	J_{xx}=0.016, J_{yy}=0.032, J_{zz}=0.027
3	m_3=150.3	m_3=150.3	J_{xx}=4.1, J_{yy}=9.2, J_{zz}=9.2	J_{xx}=4.1, J_{yy}=9.2, J_{zz}=9.2

Table 4 Numerical values for the hydraulic system parameters

Parameter	Value	Parameter	Value
Relief valve preset pressure, p_{set}	9 MPa	Drain pressure, p_0	0
Supply pressure, p_s	8 MPa (slewing), 18 MPa (luffing)	Opening and closing time of the directional valve	0.05 s
Fluid bulk modulus, β	1.32×10^9 Pa	Orifice discharge coefficient, C_d or C_{dv}	0.62
Relief valve regulation range, p_{reg}	0.5 MPa	Hydraulic cylinder strokes	l_1=0.5 m, l_2=0.38 m
Valve pressure at maximum opening, p_{max}	9.5 MPa	Radius of the pinion, R	0.12 m
Fully open relief valve passage area, A_{max}	1.2×10^{-4} m²	Direction control valve area gradient, w	0.011 m
Constant oil volumes	$V_0^1 = 18.2\times10^{-6}$ m³, $V_0^2 = 42.9\times10^{-6}$ m³	The maximum direction control valve opening, $x_v^{max}(t)$	0.5×10^{-3} m
Piston areas	S_1=1.96×10^{-3} m², S_2=7.69×10^{-3} m², S_3=3.04×10^{-3} m²	Viscous friction coefficients	b_1=1.2×10^6 N·s/m, b_2=2.2×10^6 N·s/m
Fluid density, ρ	855 kg/m³		
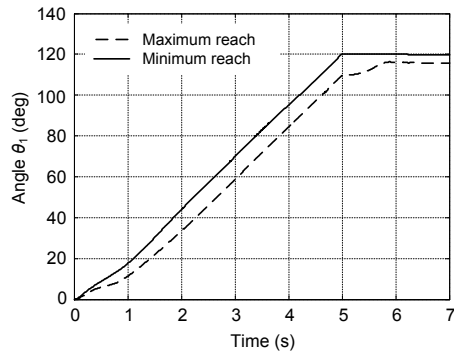
Fig. 7 Slewing angle θ_1
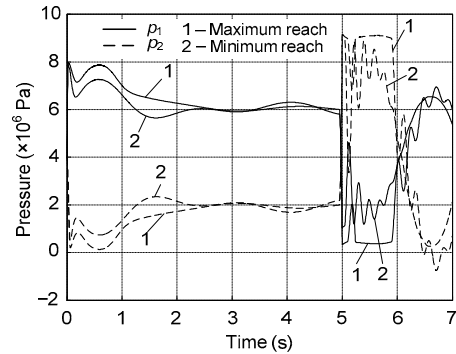
Fig. 9 Hydraulic cylinder pressure
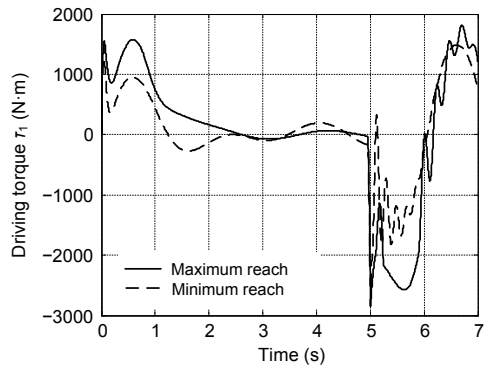
Fig. 8 Driving torque τ_1 exerted at the first link
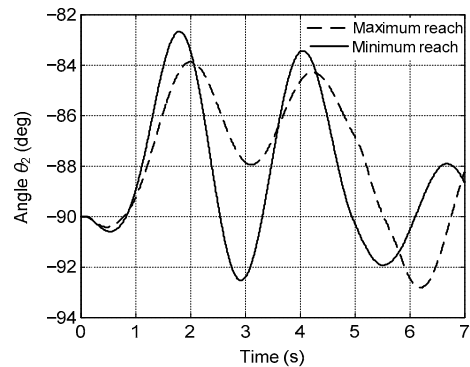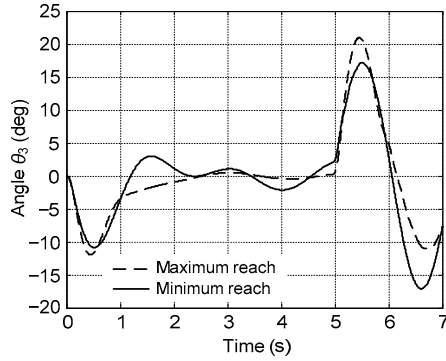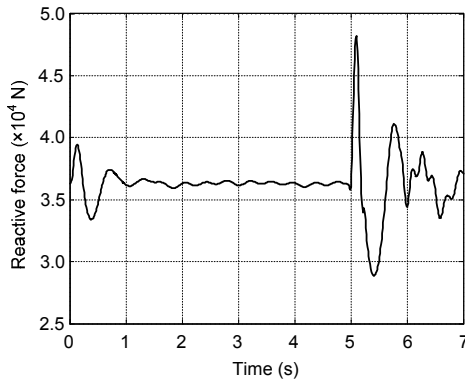

Fig. 10 Angle θ_2

Fig. 11 Angle θ_3

Fig. 12 Reactive force in the forearm hydraulic cylinder at the maximum reach

analysis a convenient process, and the time history of forces and moments in each joint can be easily computed. The reactive forces in the hydraulic actuators present particular interest, as they are important for the hydraulic driving system and the design of the mechanical structure. Using this approach, the equivalent torque M in the rotational joint, connecting the arm and the forearm, is computed. The mapping $M(F)$ of the forearm hydraulic cylinder force F to the joint torque M is established using the principle of the virtual work (Greenwood, 1977), which allows the formulation of the required equations without considering the forces generated in the linkage joints. Applying this principle to the forearm driving mechanism, the layout of which is shown in Fig. 13, one can write

$$M = -F\frac{L\sin(\varphi_1-\varphi_2)\sin(\varphi_3-\varphi_4)}{\sin(\varphi_2-\varphi_3)}, \qquad (32)$$

where all angles are measured from the arm axis *n-n*. The computed reactive force in the forearm hydraulic

cylinder during the slewing motion is shown in Fig. 12.

It will be shown later in Fig. 19 that the simulation data (Fig. 12) are overlapped with the experimental data for the reactive force, calculated from the experimentally measured pressures.
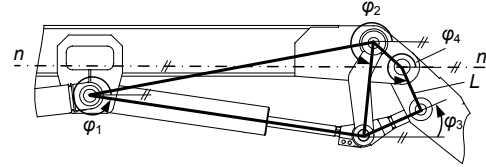

Fig. 13 Forearm hydraulic cylinder layout

3.2 Luffing case simulation

To simulate the link motion for this case, the same set of differential equations with the corresponding values from Table 2 is used. The initial conditions for the generalized coordinates are set to $\theta_1(0)=-15°$, $\theta_2(0)=-105°$, and $\theta_3(0)=-15°$. The lifting process starts with a payload laying on the ground and a slack suspension cable. The overall duration of the simulation is 20 s. The process corresponds to the following sequence of motions performed by the hydraulic control valve activation: (1) boom raising, from initial angle $\theta_1=-15°$ to angle 22.5°; (2) holding in the upper position for 2 s; (3) boom lowering to the initial position. The time evolutions of payload swinging angles θ_2 and θ_3 are shown in Figs. 14 and 15, respectively. The simulation of the boom rotation angle θ_1 will be given later in Fig. 17, while the simulations of the corresponding pressures p_1 and p_2 in the arm hydraulic cylinder will be shown in Fig. 18.

4 Experimental setup and validation of the mathematical model

The validation of the mathematical model is conducted by comparison between the simulation and the experimental data. Fig.16 shows a view of the experimental setup, whose main elements are the rotating column, the arm, the forearm, and the hydraulic power unit. It is equipped with sensors for measuring six different quantities as follows: (1) the pressures at the cap end and at the rod end of the arm driving cylinder; (2) the pressures at the cap end and

at the rod end of the forearm driving cylinder; (3) the current displacements of the arm and the forearm driving cylinders. For the displacement measurement, two linear variable inductance transducers are used,
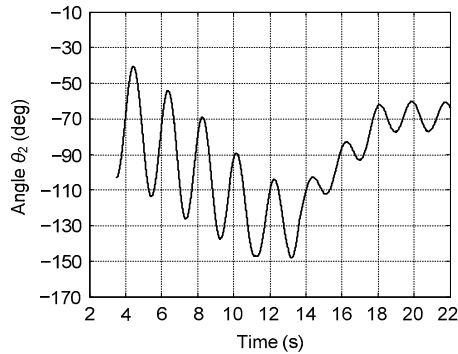

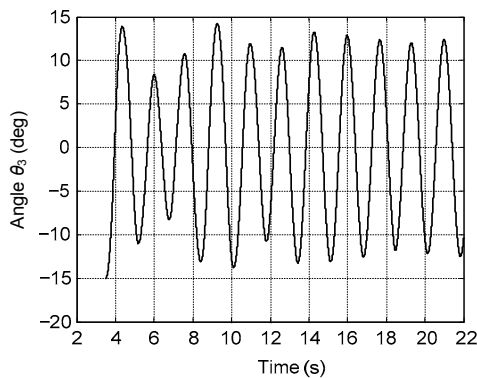**Fig. 14 Angle θ_2**
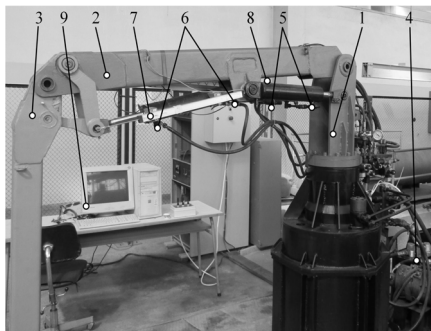

Fig. 15 Angle θ_3

Fig. 16 A view of the experimental setup and sensor placement

1: rotating column; 2: arm; 3: forearm; 4: hydraulic power unit; 5: sensors for measuring the pressures at the cap end and at the rod end of the arm driving cylinder; 6: sensors for measuring the pressures at the cap end and at the rod end of the forearm driving cylinder; 7: sensor for measuring the current displacement of the arm driving cylinder; 8: sensor for measuring the current displacement of the forearm driving cylinder; 9: computer measurement system

attached to the body and the rod couplings of the hydraulic cylinders, while for pressure measurement, four pressure sensors to measure absolute pressures are used. Analog outputs from the sensors are converted to digital ones by analog-to-digital converter (National Instruments 8 inputs, 14 bits) and are sent to a computer measurement system, where a computer program DASYLab 11 is used for initial processing and visualization of data.

The experimental data overlapped with the numerical simulation results are shown in Figs. 17 and 18 for the luffing case, and in Fig. 19 for the slewing case.
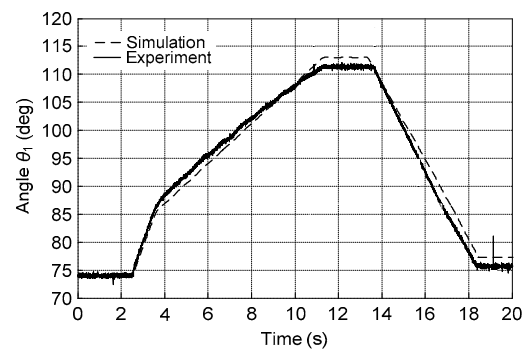

Fig. 17 Time history of the boom rotation angle θ_1 for the luffing case

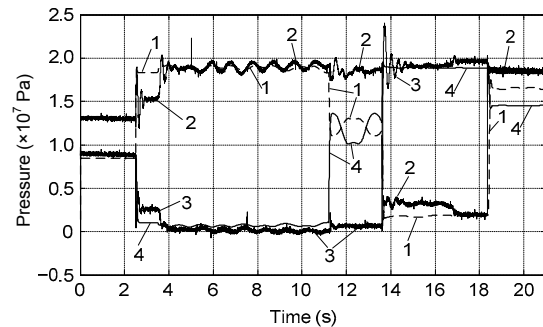**Fig. 18 Pressures in the boom hydraulic cylinder for the luffing case**

1: simulation data for p_1; 2: experimental data for p_1; 3: experimental data for p_2; 4: simulation data for p_2

5 Discussion

The results from the numerical simulation show that the driving torque (force) of the hydraulic actuators depends mostly on the parameters of the fluid flow and that the inertial properties of the system have
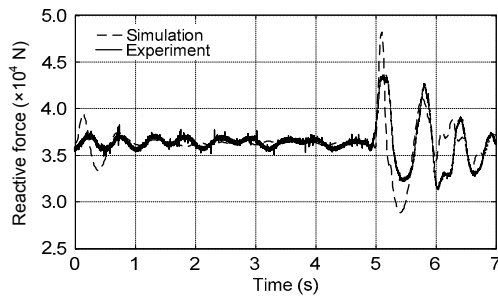
Fig. 19 Reactive force in the forearm hydraulic cylinder for the slewing case

little influence upon its motion. This is clear from Fig. 7 (for the slewing case), where for the minimum reach and the maximum reach, angle θ_1 reaches nearly the same value at the end of the simulation time (about 3.3% difference). Nevertheless, as might be expected, an increase of the mass moment of inertia of the mechanical system leads to a decrease of the rotational acceleration. This can be explained having in mind the results shown in Fig. 8, where the driving moment τ_1 as a function of time is given. The constant supply pressure causes a slight increase in the driving torque for the maximum reach, when a larger inertial force is opposed.

The sudden closure of the directional valve at the end of rotation ($t=5$ s) causes a significant rise of pressure in the hydraulic circuit, as shown in Fig. 9 the variation in pressure for both volumes of the hydraulic actuator. The suddenly increased pressure after closure of the valve produces a flow through the relief valves. This flow restricts the pressure in the cylinder equal to the valve preset pressure, but hampers the exact positioning of the crane. The effect is clearly visible in Fig. 7 (see the curve for the maximum reach), which shows a slight increase in angle θ_1 after the closure of the direction control valve at $t=5$ s. Fig. 9 also shows that the payload swinging induces an additional pressure variation in the hydraulic circuit, which cannot be neglected. Such a variation is present during the rotation phase (0–5 s), and also after the directional valve closure (5–7 s). This is confirmed by the results of the driving moment shown in Fig. 8. As can be seen in Fig. 9, the pressures in both hydraulic cylinder chambers are symmetrical.

Because of the rotation of the mechanical system, tangential and radial accelerations occur, leading to the payload swinging about two mutually perpendicular axes. Swinging angles of the payload (angles θ_2 and θ_3) are shown in Figs. 10 and 11. It can be seen that the nature of the swings does not depend very much on the boom configuration; the maximum amplitudes of the swinging angles in both the minimum reach and the maximum reach are about 6°–8° for θ_2 and 18°–20° for θ_3. The actual swing in the plane perpendicular to that of the boom (Fig. 11) damps relatively quickly after the initial acceleration and starts after the valve closure. The swing amplitudes depend on the cable length. Relatively large amplitude values give rise to extensive inertial loads as well as fatigue and reliability problems.

The luffing case simulates lifting a payload off the ground with some initial speed, which is one of the reasons for considerable payload swinging, especially during the lifting phase (Figs. 14 and 15). From Fig. 18 one can see that the variations in cylinder pressure induced by payload swinging are relatively small and this can be related to the much higher static component of pressure compared with the dynamic one in the hydraulic cylinder. As with the slewing case, pressures in the actuator's volumes are nearly symmetrical. Moreover, Fig. 18 reveals a considerable difference between the experimentally measured and simulated pressures, which is observed during the period of holding the boom in the upper position (in time interval 11.5–13.5 s). Nevertheless, the comparison of the results and the good correlation between the experimental data and simulation results allow us to conclude that the adopted mathematical model may confidently be used to simulate the dynamic problems present.

From the range of variation of the reactive force in the forearm hydraulic cylinder during slewing motion (Figs. 12 and 19), it might be concluded that a dynamic factor of 1.3–1.4 should be taken into account when the metal frame and a hydraulic driving system are designed. Similarly, the graph of the driving torque (Fig. 8) shows considerable dynamic loading onto the rack and pinion driving mechanism and metal frame elements due to the payload swinging induced during motion.

6 Conclusions

The design process for a hydraulic crane is highly iterative and a number of iterations are needed

to achieve a satisfactory design. The design of a system, containing subsystems from hydraulic and mechanical domains is difficult, and the modeling technique must take into account their interaction in operational performance. The hydraulic actuators, controlling the moving crane elements, have their own dynamics due to the presence of inertial parameters of their elements and the compressibility of the hydraulic oil. The internal forces, which arise in the mechanical system during performance of typical operations, and the pressures and flows in the hydraulic system, are important for the reliability and strength calculations of the crane elements.

We have studied issues related to the development of a nonlinear dynamical model of a hydraulic crane operating with freely suspended payload. Among many important aspects that might be investigated, the simultaneous modeling and simulation of subsystems from different physical domains has been performed. The conducted investigation clearly shows that payload swinging during the motion of a hydraulic crane strongly influences the dynamic processes in the crane mechanical system and the hydraulic driving system itself, and thus cannot be neglected in the system design. The main direction for the improvement of the system performance is the implementation of a control system for minimizing the payload swinging, especially for the slewing motion. The performed validation of the developed dynamical model shows its applicability for the study of the hydraulic crane motion simulation, considering large angles of payload swinging and taking into account the hydraulic driving system dynamics. Although the two typical motions have been considered separately, the modeling approach used is suitable for study of the crane general motion including the simultaneous link motion.

References

Abdel-Rahman, E.M., Nayfeh, A.H., Masoud, Z.N., 2003. Dynamics and control of cranes: a review. *Journal of Vibration and Control*, **9**(7):863-908.
http://dx.doi.org/10.1177/1077546303009007007

Akers, A., Gassman, M., Smith, R., 2006. Hydraulic Power Systems Analysis. CRC Press, USA, p.77-100.

Chin, C., Nayfeh, A.H., Abdel-Rahman, E., 2001. Nonlinear dynamics on a boom crane. *Journal of Vibration and Control*, **7**(2):199-220.
http://dx.doi.org/10.1177/1077546301007000204

Craig, J.J., 2005. Introduction to Robotics: Mechanics and Control (3rd Edition). Pearson Prentice Hall, p.171-172.

Devesse, W., 2012. Slew Control Methods for Tower Cranes. MS Thesis, KTH Industrial Engineering and Management Machine Design, Stockholm, Sweden.

Divisiev, V., 1986. Essential Hoisting Machines. Technika, Sofia, p.45-49 (in Bulgarian).

Greenwood, D.T., 1977. Classical Dynamics. Prentice Hall, p.13-25.

Grigorov, B., 2013. A generalized Newton-Euler algorithm for dynamic simulation of robot-manipulators with revolute joints. *Recent*, **14**(2):99-105.

Gruening, T., Kunze, G., Katterfeld, A., 2010. Simulating the working process of construction machines. 3rd International Conference & Exhibition BulkSolids, p.180-189.

Gudarzi, M., 2016. Reliable robust controller for half-car active suspension systems based on human-body dynamics. *Facta Universitatis Series: Mechanical Engineering*, **14**(2):121-134.

Hartenberg, R.S., Denavit, J., 1955. A kinematic notation for lower pair mechanisms based on matrices. *Journal of Applied Mechanics*, **22**(2):215-221.

Jerman, B., 2006. An enhanced mathematical model for investigating the dynamic loading of a slewing crane. *Proceedings of the Institution of Mechanical Engineers, Part C: Journal of Mechanical Engineering Science*, **220**(4):421-433.
http://dx.doi.org/10.1243/09544062C08205

Jovanovic, V., Janosevic, D., Petrovic, N., 2014. Experimental determination of bearing loads in rotating platform drive mechanisms of hydraulic excavators. *Facta Universitatis Series: Mechanical Engineering*, **12**(2):157-169.

Ju, F., Choo, Y., Cui, F.S., 2006. Dynamic response of tower crane induced by the pendulum motion of the payload. *International Journal of Solids and Structures*, **43**(2):376-389.
http://dx.doi.org/10.1016/j.ijsolstr.2005.03.078

Lawrence, J., Singhose, W., 2010. Command shaping slewing motions for tower cranes. *Journal of Vibration and Acoustics*, **132**(1):011002.
http://dx.doi.org/10.1115/1.3025845

Linjama, M., Virvalo, T., 1999. Low-order dynamic model for flexible hydraulic cranes. *Proceedings of the Institution of Mechanical Engineers, Part I: Journal of Systems and Control Engineering*, **213**(1):11-22.
http://dx.doi.org/10.1243/0959651991540340

Marinković, Z., Marinković, D., Petrović, G., *et al.*, 2012. Modeling and simulation of dynamic behaviour of electric motor driven mechanisms. *Tehnički Vjesnik*, **19**(4):717-725.

Marinovic, I., Sprecic, D., Jerman, B., 2012. A slewing crane payload dynamics. *Tehnički Vjesnik*, **19**(4):907-916.

Palis, F., Palis, S., 2008. High performance tracking control of automated slewing cranes. *In*: Balaguer, C., Abderrahim, M. (Eds.), Robotics and Automation in Construction. InTech, p.187-198.
http://dx.doi.org/10.5772/5851

Papadopoulos, E., Sarkar, S., 1997. The dynamics of an articulated forestry machine and its applications. IEEE International Conference on Robotics and Automation, p.323-328.
https://dx.doi.org/10.1109/ROBOT.1997.620058

Pavlovic, J., Jovanovic, M., Miloevic, A., 2014. Optimal synthesis of the manipulator using two competitive methods. *Facta Universitatis Series: Mechanical Engineering*, **12**(1):61-72.

Ren, H.L., Wang, X.L., Hu, Y.J., *et al.*, 2008. Dynamic response analysis of a moored crane-ship with a flexible boom. *Journal of Zhejiang University-Science A*, **9**(1):26-31.
https://dx.doi.org/10.1631/jzus.A071308

Sicklinger, S., Belsky, V., Engelmann, B., *et al.*, 2014. Interface Jacobian-based co-simulation. *International Journal for Numerical Methods in Engineering*, **98**(6):418-444.
https://dx.doi.org/10.1002/nme.4637

Sun, G., Liu, J., 2006. Dynamic responses of hydraulic crane during luffing motion. *Mechanism and Machine Theory*, **41**(11):1273-1288.
https://dx.doi.org/10.1016/j.mechmachtheory.2004.07.014

Sun, G., Kleeberger, M., Liu, J., 2005. Complete dynamic calculation of lattice mobile crane during hoisting motion. *Mechanism and Machine Theory*, **40**(4):447-466.
https://dx.doi.org/10.1016/j.mechmachtheory.2004.07.014

Troha, S., Milovančević, M., Kuchak, A., 2015. Software testing of the rall vehicle dynamic characteristics. *Facta Universitatis Series: Mechanical Engineering*, **13**(2):109-121.

Vaynson, A., 1989. Hoisting Machines. Machinostroenie, Moscow, p.124-134 (in Russian).

Vukobratovic, M., Potkonjak, V., 1982. Dynamics of Manipulation Robots: Theory and Application. Springer-Verlag, Berlin, Germany, p.87-116.

Zill, D., Cullen, M., 2006. Advanced Engineering Mathematics. Jones & Bartlett Publishers, p.319.

中文概要

题　目：液压起重机操作自由悬浮载荷的动态特性

目　的：对载有自由悬浮载荷的液压驱动起重机的动态特性分别在升降运动和回转运动两种工况下进行研究，建立动力学模型并验证其正确性。

创新点：1. 为了简化任务，将两种运动分开讨论。一次只考虑一种运动，把起重机看作具有三个转动关节连接的运动链；2. 为起重臂的运动问题构造微分方程，使用了通用的牛顿-欧拉算法；3. 对运动和动力模型进行仿真，得到摆动角度、液压压强和连接作用力随时间的变化曲线，并通过实验进行了验证。

方　法：1. 建立系统的运动和动力模型，分别对回转运动和升降运动两种工况下的液压缸压强进行推导；2. 在两种工况下，对起重臂转角、液压缸压力和最大行程前臂液压缸反作用力进行仿真计算；3. 将实验获得的有关参数的曲线与仿真得到的曲线进行对比，验证模型的正确性。

结　论：1. 在液压起重机运动期间悬浮载荷的摆动对起重机的机械系统和液压驱动系统本身具有强烈的影响，所以在系统设计中不能忽视；2. 系统性能提升的主要方向是安装控制系统以减小载荷摆动（特别是在起重机回转运动时）；3. 本文建立的考虑了负载的大角度摆动和液压驱动系统的动力学模型得到了验证，表明其对起重机运动仿真的适用性。尽管分开考虑了两种典型运动，但所用的建模方法还是适合对起重机一般运动的研究。

关键词：液压起重机；载荷摆动；牛顿欧拉方法；液压驱动